Geophysical Prospecting, 1999, **47**, 1015–1029

GPR modelling by the Fourier method: improvement of the algorithm[1]

J.M. Carcione,[2] G. Lenzi[3] and S. Valle[4]

Abstract

We improve two aspects of the modelling scheme for the simulation of electromagnetic radio waves, based on the Fourier pseudospectral method.

When there are large contrasts in the material properties, use of the standard algorithm (regular grid) causes a series of artefacts, as, for instance, ringing and acausal events. These problems, due to the non-locality of the differential operator, are solved by using the staggered Fourier method (staggered grid).

Realistic radiation patterns can be obtained from simple combinations of magnetic and electric sources. If the directivity pattern of the antenna is known, from either a finite-difference simulation or an analytic evaluation or an experimental characterization, it can then be simulated by a composite-source concept. This effective source is implemented in the modelling algorithm by means of a perturbation technique, which first computes the intensity and directional spectra of the single electromagnetic sources. Their location is optimized to obtain the best fit with a minimum number of sources. The approach is, in principle, valid for the far-field radiation pattern of the antenna.

Introduction

In the modelling of ground-penetrating radar (GPR) surveys, computation of the spatial derivatives using non-local differential operators, as in the Fourier pseudospectral method, may cause strong numerical artefacts in the form of non-causal ringing. This situation occurs when regular grids are used. The problem is approached using a staggered pseudospectral technique, with a different scheme for each rheological relationship. The nature and the causes of acausal ringing in regular-grid methods and the reasons why staggered-grid methods eliminate this problem have been explained by Fornberg (1990) and Özdenvar and McMechan (1996, 1997). Thus, the objective here

[1] Received May 1998, revision accepted January 1999.
[2] Osservatorio Geofisico Sperimentale, PO Box 2011, Opicina, 34016 Trieste, Italy.
E-mail: jcarcione@ogs.trieste.it
[3] ISMES, S.p.A., Via Pastrengo 9, 24068 Seriate (BG), Italy.
[4] Politecnico di Milano, Dipartimento di Elettronica e Informazione, Piazza Leonardo da Vinci 32, 20133 Milano, Italy.

is not to propose a new method, but to develop the algorithm for Maxwell's equation, including dielectric relaxation and out-of-phase electric currents.

The computation of realistic synthetic radargrams by grid methods requires a proper simulation of the GPR antenna radiation pattern. Semi-analytical solutions of antenna radiation over a dielectric half-space, based on the far-field approximation, have been given by Engheta, Papas and Elachi (1982) and Smith (1984), while Harrington (1968), Turner (1994) and Chew (1995) used the method of moments.

In principle, it is possible to obtain a precise numerical evaluation of the transient field radiation. Maloney, Smith and Scott (1990), Bourgeois and Smith (1996), Roberts and Daniels (1997) and Bergmann (1998) computed the directivity properties of GPR antennae using a finite-difference time-domain (FDTD) method. However, the explicit implementation of the antenna characteristics (geometry and material properties) for different heights relative to the ground requires the use of an extended numerical mesh. For practical purposes it is convenient to simulate the radiation pattern of the transmitting antenna by an equivalent approach. If the directivity pattern of the antenna is known, from either a finite-difference simulation or an analytic evaluation (Annan 1973; Arcone 1995) or an experimental characterization (e.g. Wensink *et al.* 1990; Bernabini *et al.* 1995), it can then be simulated by the method developed by Carcione (1998).

The EM radiation of a GPR antenna is affected by the geometrical and physical characteristics of the antenna. In order to simulate the radiation pattern with grid methods, without explicit modelling of these features, an equivalent solution is obtained by using a composite-source concept. The 2D analytic solution corresponding to magnetic and electric sources located at the same gridpoint is computed. This solution constitutes a basis for the construction of a composite source located in a small region of the numerical mesh (Carcione 1998). In this way, realistic radiation patterns can be obtained from simple combinations of magnetic and electric sources.

Carcione (1998) described the forward problem, i.e. he obtained the analytical solution for the far-field electromagnetic radiation. Here, we estimate the composite-source parameters by fitting the solution to a given radiation pattern. Moreover, the use of time functions instead of a single amplitude weight allows the simulation of amplitude and phase patterns. An inversion technique, based on a perturbation method, which uses fictitious monopole and dipole sources was presented by Landrø, Mittet and Sollie (1993) for simulating marine seismic source signatures in a coarse-grid finite-difference scheme. We adapt this method to the electromagnetic problem in order to find the fictitious magnetic and electric sources that better simulate the GPR antenna radiation pattern.

Maxwell's equations

The TM differential equations for one Debye relaxation mechanism and out-of-phase

electric currents can be written as (Carcione 1996)

$$\begin{aligned}
&\partial_x E_z - \partial_z E_x = \mu \partial_t H_y + M_y,\\
&-\partial_z H_y = \sigma_e^{\infty} E_x + \epsilon_e^{\infty} \partial_t E_x + \epsilon^0 e_x + J_x,\\
&\partial_x H_y = \sigma_e^{\infty} E_z + \epsilon_e^{\infty} \partial_t E_z + \epsilon^0 e_z + J_z,\\
&\partial_t e_x = -\omega_0 a \left[e_x + \omega_0 a \left(1 - a^2\right) E_x \right],\\
&\partial_t e_z = -\omega_0 a \left[e_z + \omega_0 a \left(1 - a^2\right) E_z \right],
\end{aligned} \tag{1}$$

where E_x, E_z, H_y, e_x and e_z are field components, M_y, $\mathcal{J}_x$ and $\mathcal{J}_z$ are external sources, μ is the magnetic permeability,

$$\epsilon_e^{\infty} = \epsilon^{\infty} + \xi \sigma^0 \tag{2}$$

and

$$\sigma_e^{\infty} = \sigma^0 + \omega_0 a (1 - a^2) \epsilon^0 \tag{3}$$

are the effective optical permittivity and conductivity, respectively, with ϵ^{∞} and ϵ^0 denoting the optical and static permittivities, σ^0 denoting the static conductivity, ξ denoting a relaxation time quantifying the out-of-phase currents, ω_0 denoting the central frequency of the Debye relaxation, and $a = \sqrt{\epsilon^{\infty}/\epsilon^0}$.

A better parametrization of the Debye peak considers the central frequency f of the peak, and the minimum quality factor Q. We have

$$\omega_0 = 2\pi f, \qquad \epsilon^0 = \epsilon^{\infty} \frac{\sqrt{Q^2 + 1} + 1}{\sqrt{Q^2 + 1} - 1}. \tag{4}$$

Calculation of the spatial derivatives for staggered grids

On a regular grid, the field components and material properties are represented at each gridpoint, while on a staggered grid, the locations are indicated in the following mesh:

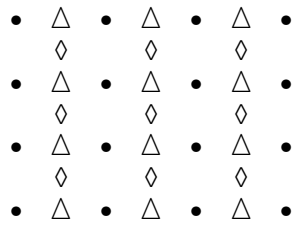

such that

$$\begin{array}{lll}
\bullet & (i,j) & E_z,\ J_z,\ e_z,\ \epsilon_e^{\infty},\ \epsilon^0,\ \sigma_e^{\infty},\ \omega_0,\ a\\
\Diamond & \left(i + \frac{1}{2}, j + \frac{1}{2}\right) & E_x,\ J_x,\ e_x,\ \epsilon_e^{\infty},\ \epsilon^0,\ \sigma_e^{\infty},\ \omega_0,\ a\\
\triangle & \left(i + \frac{1}{2}, j\right) & H_y,\ M_y,\ \mu.
\end{array} \tag{5}$$

Material properties at half-gridpoint ◊ locations are computed by averaging the values defined at • locations. The averaging is chosen in such a way as to reduce the error between the numerical solution corresponding to an interface aligned with the numerical grid and the equivalent solution obtained with a regular grid. The tests show that the values should be computed by a simple arithmetic averaging. For instance, at ◊ locations,

$$a\left(i+\frac{1}{2},j+\frac{1}{2}\right)=\frac{1}{4}\left[a(i+1,j+1)+a(i+1,j)+a(i,j+1)+a(i,j)\right].$$

For computing μ at $\triangle$ locations, we first compute μ at ◊ points, and then average between these values and the • values. This gives

$$\mu\left(i+\frac{1}{2},j\right)=\frac{1}{8}\{3\mu(i,j)+3\mu(i+1,j)+\frac{1}{2}[\mu(i,j+1)$$
$$+\mu(i,j-1)+\mu(i+1,j+1)+\mu(i+1,j-1)]\}.$$

A review of the artefacts and numerical instabilities caused by the Fourier differential operator when using a regular grid has been given by Özdenvar and McMechan (1996). The use of a staggered grid overcomes these problems. The first-order derivative computed with the staggered differential operator is evaluated between gridpoints, using even-based Fourier transforms. The standard first-order differential operator along the x-direction is

$$D_x\phi=\sum_{k_x=0}^{k_x(N)}\mathrm{i}k_x\tilde{\phi}(k_x)\exp(\mathrm{i}k_x x), \tag{6}$$

where $\tilde{\phi}$ is the Fourier transform of ϕ and $k_x(N)$ is the Nyquist wavenumber. Staggered operators, which evaluate the derivatives between gridpoints, are given by

$$D_x^{\pm}\phi=\sum_{k_x=0}^{k_x(N)}\mathrm{i}k_x\exp(\pm\mathrm{i}k_x\Delta x/2)\tilde{\phi}(k_x)\exp(\mathrm{i}k_x x), \tag{7}$$

where Δx is the grid spacing.

The staggered Maxwell equations can be written as

$$\begin{array}{ll}
\triangle & D_x^+E_z-D_z^-E_x=\mu\partial_t H_y+M_y\\
\lozenge & -D_z^+H_y=\sigma_e^{\infty}E_x+\epsilon_e^{\infty}\partial_t E_x+\epsilon^0 e_x+J_x\\
\bullet & D_x^-H_y=\sigma_e^{\infty}E_z+\epsilon_e^{\infty}\partial_t E_z+\epsilon^0 e_z+J_z\\
\lozenge & \partial_t e_x=-\omega_0 a\left[e_x+\omega_0 a\left(1-a^2\right)E_x\right]\\
\bullet & \partial_t e_z=-\omega_0 a\left[e_z+\omega_0 a\left(1-a^2\right)E_z\right].
\end{array} \tag{8}$$

Simulation of the antenna radiation pattern

The radiation pattern of any antenna can be obtained by summing the contributions of many single sources, each with its own time function. Consider a composite source

located in a rectangular region of the mesh, where the material properties are homogeneous. If the size of the rectangle is $2L_x \times 2L_z$ (measured in gridpoints) and the respective grid spacings are dx and dz, the total magnetic field can be expressed as (Carcione 1998),

$$H_y(x,z,\omega) = \pi\omega \sum_{i=-L_x}^{L_x} \sum_{j=-L_z}^{L_z} \{ I_{\mathrm{M}}(i,j,\omega) \mathrm{H}_0^{(2)}(\alpha_{ij}) + \mathrm{i}\mu\omega[(x-idx) I_Z(i,j,\omega) - (z-jdz) I_X(i,j,\omega)] \alpha_{ij}^{-1} \mathrm{H}_1^{(2)}(\alpha_{ij}) \} \times \delta(x-idx)\delta(z-jdz), \quad (9)$$

where $I_{\mathrm{M}}(i,j,\omega)$, $I_{\mathrm{X}}(i,j,\omega)$ and $I_{\mathrm{Z}}(i,j,\omega)$ are the magnetic and electric source spectra at the gridpoint (i,j), respectively, $\mathrm{H}_0^{(2)}$ and $\mathrm{H}_1^{(2)}$ are the Hankel functions of the second kind, and

$$\alpha_{ij} = \omega\sqrt{\mu\epsilon^*}[(x-idx)^2 + (z-jdz)^2]^{1/2}, \quad (10)$$

with ϵ^* being complex and dependent on frequency, ω_0, ϵ^0, ϵ^∞, ξ and σ^0 (Carcione 1996, 1998).

The source spectrum can be computed by inverting (9), taking $H_y(x,y,\omega)$ as the Fourier transform of the data. The problem can be solved with a perturbation technique (e.g. Landrø *et al.* 1993), by first inverting (9) for the magnetic sources and then for the electric sources. Hence, in step one, we have the linear system

$$\mathbf{H}_{\mathrm{obs}} = \boldsymbol{\Gamma}\mathbf{I}_{\mathrm{M}}, \quad (11)$$

where $\mathbf{H}_{\mathrm{obs}}$ is a vector of length $n_{\mathrm{d}} \times n_{\mathrm{f}}$ where n_{d} is the number of experimental points and n_{f} is the number of frequencies; $\boldsymbol{\Gamma}$ is a matrix of dimension $(n_{\mathrm{d}} \times n_{\mathrm{f}}) \times (n_{\mathrm{sM}} \times n_{\mathrm{f}})$ where n_{sM} is the number of magnetic sources, and $\mathbf{I}_{\mathrm{M}}$ is the unknown vector of magnetic sources, of length $n_{\mathrm{sM}} \times n_{\mathrm{f}}$. The solution to (11) can be written as

$$\mathbf{I}_{\mathrm{M}} = [\,\boldsymbol{\Gamma}^*\,\boldsymbol{\Gamma}]^{-1}\,\boldsymbol{\Gamma}^*\mathbf{H}_{\mathrm{obs}}, \quad (12)$$

where $\boldsymbol{\Gamma}^*$ denotes the adjoint (complex transpose) of $\boldsymbol{\Gamma}$. Then, the difference between the modelled field and the data,

$$\Delta\mathbf{H} = \mathbf{H}_{\mathrm{obs}} - \boldsymbol{\Gamma}\mathbf{I}_{\mathrm{M}}, \quad (13)$$

is used to invert (11) for one of the two types of electric source, as follows:

$$\mathbf{I}_{X(Z)} = [\,\boldsymbol{\Gamma}^*\,\boldsymbol{\Gamma}]^{-1}\,\boldsymbol{\Gamma}^*\Delta\mathbf{H}, \quad (14)$$

where $\mathbf{I}_{X(Z)}$ is the vector of electric sources of length $n_{\mathrm{s}X} \times n_{\mathrm{f}}$ ($n_{\mathrm{s}Z} \times n_{\mathrm{f}}$), and $n_{\mathrm{s}X}$ ($n_{\mathrm{s}Z}$) is the number of electric sources in the x-(z-)direction. Proceeding as before, we compute the new difference field,

$$\Delta\mathbf{H} = \mathbf{H}_{\mathrm{obs}} - \boldsymbol{\Gamma}[\mathbf{I}_{\mathrm{M}}, \mathbf{I}_{X(Z)}] \quad (15)$$

and we then determine the other type of electric source. Note that the number of unknowns, and therefore the number of sources, depends on the number of

independent data (i.e. the number of traces collected in sufficiently different positions). An iterative approach is required to optimize the number of sources and their corresponding positions. Usually a 3×3 grid centred on the antenna position supplies enough sources (even for complex patterns), provided that the inversion is well constrained. We start with all the available sources and gradually remove those that do not contribute significantly to the radiation. Physical considerations and the radiation patterns shown in Fig. 6 can aid the design of starting configurations with a reduced number of sources. This approach is essential in the case of a shortage of input data, in order to avoid ill-conditioned inversion systems. The optimum solution will be a trade-off between the accepted error, the amount of input data and the number of sources.

Numerical examples

Staggered mesh

Let us consider an interface separating two different media, denoted in Table 1 by subscripts 1 and 2. Each case corresponds to a discontinuity of a given material property. We consider a regular grid of 81×81 points and a staggered grid of 80×80 points, both with a grid spacing of 7.5 cm, and a source central frequency $f = 500$ MHz for cases 1, 3, 4 and 5, and 333 MHz for case 2. Figures 1–5 compare the respective snapshots obtained from a magnetic source located 30 cm above the interface. As can be appreciated, the staggered differential operator greatly improves the modelling results by eliminating the non-causal vertical ringing and the events coming from the top and bottom of the numerical mesh.

Radiation patterns

The first set of numerical experiments tests the ability of the modelling technique to simulate the radiation patterns of magnetic and electric sources above the air/solid dielectric interface. The sources are located 5 cm from the interface and have a central frequency of 750 MHz, while the solid has a dielectric constant equal to $4\epsilon_0$. This implies that the wavelengths of the signal are 40 cm in air and 20 cm in the solid

Table 1. Material properties.

Case	μ_1 (μ_0)	ϵ_1^∞ (ϵ_0)	σ_1^0 (S/m)	Q_1	μ_2 (μ_0)	ϵ_2^∞ (ϵ_0)	σ_2^0 (S/m)	Q_2
1	4	1	0	∞	1	1	0	∞
2	1	9	0	∞	1	1	0	∞
3	4	1	0	∞	1	4	0	∞
4	1	1	0.001	∞	1	1	0.03	∞
5	1	1	0	∞	1	1	0	2

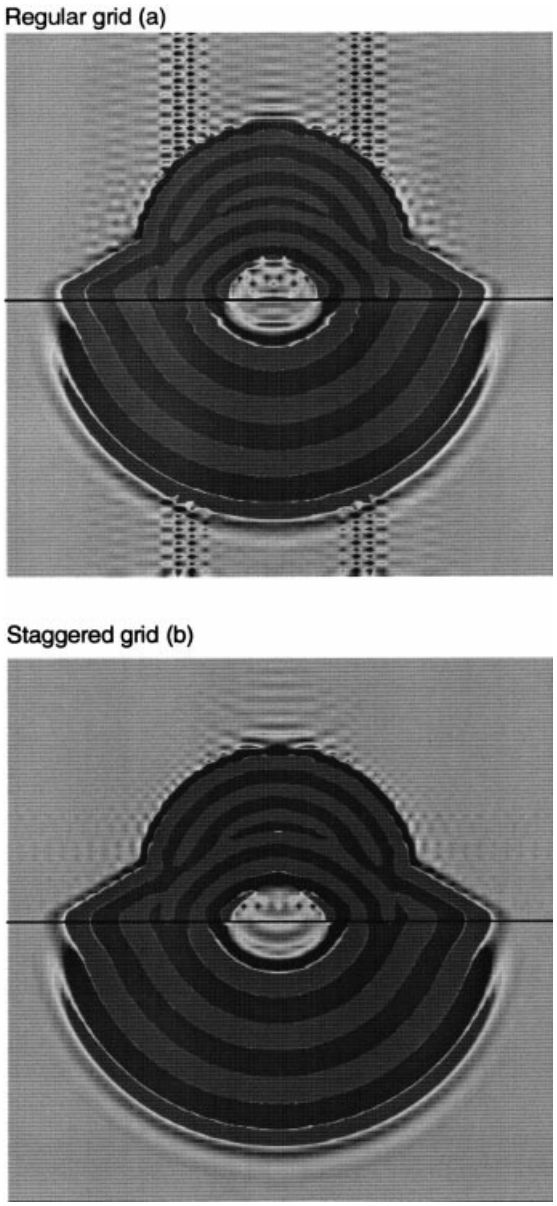

Figure 1. Snapshot of the *x*-component of the electric field at 10 ns on (a) regular and (b) staggered grids, corresponding to Case 1 in Table 1. The source, with a central frequency of 500 MHz, is 30 m above the interface. The signal-to-noise ratio in (a) is approximately 53 dB.

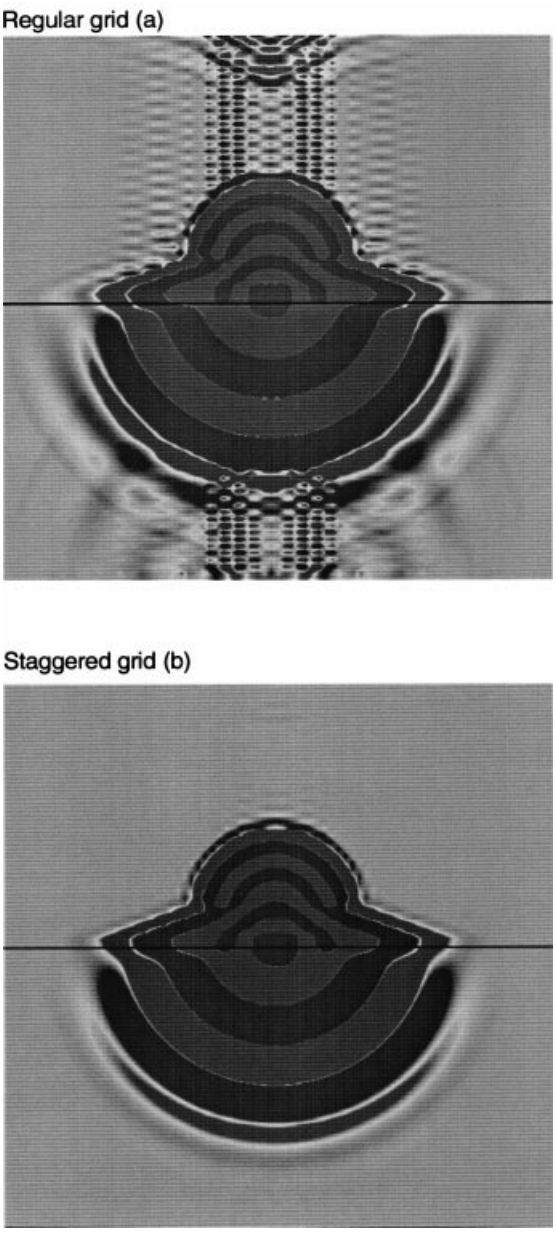

Figure 2. Snapshot of the x-component of the electric field at 10 ns on (a) regular and (b) staggered grids, corresponding to Case 2 in Table 1. The source, with a central frequency of 333 MHz, is 30 m above the interface. The signal-to-noise ratio in (a) is approximately 43 dB.

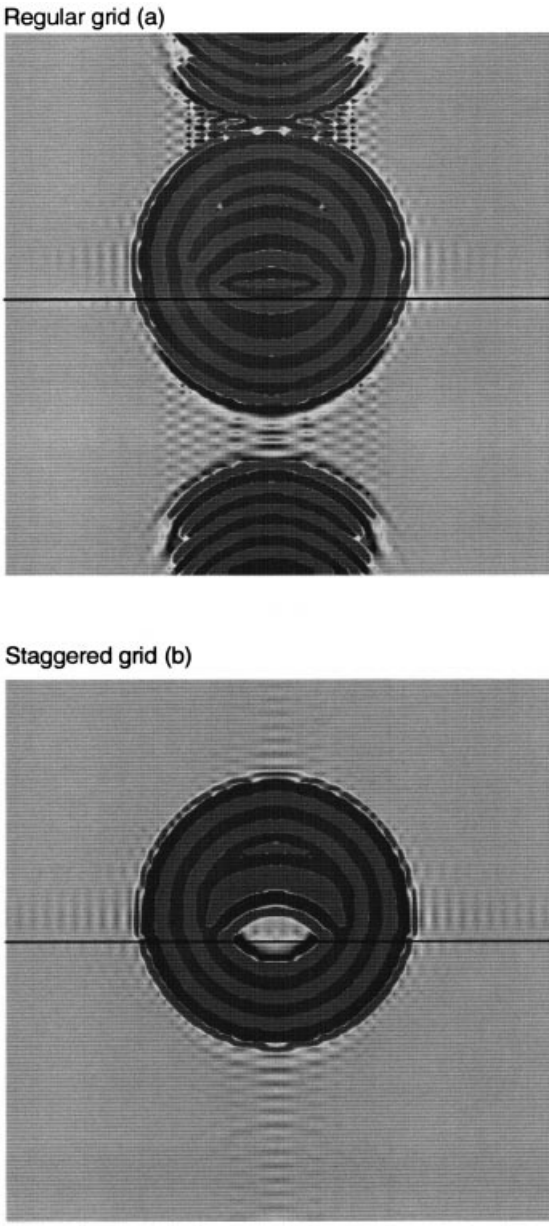

Figure 3. Snapshot of the *y*-component of the magnetic field at 10 ns on (a) regular and (b) staggered grids, corresponding to Case 3 in Table 1. The source, with a central frequency of 500 MHz, is 30 m above the interface. The signal-to-noise ratio in (a) is approximately 31 dB.

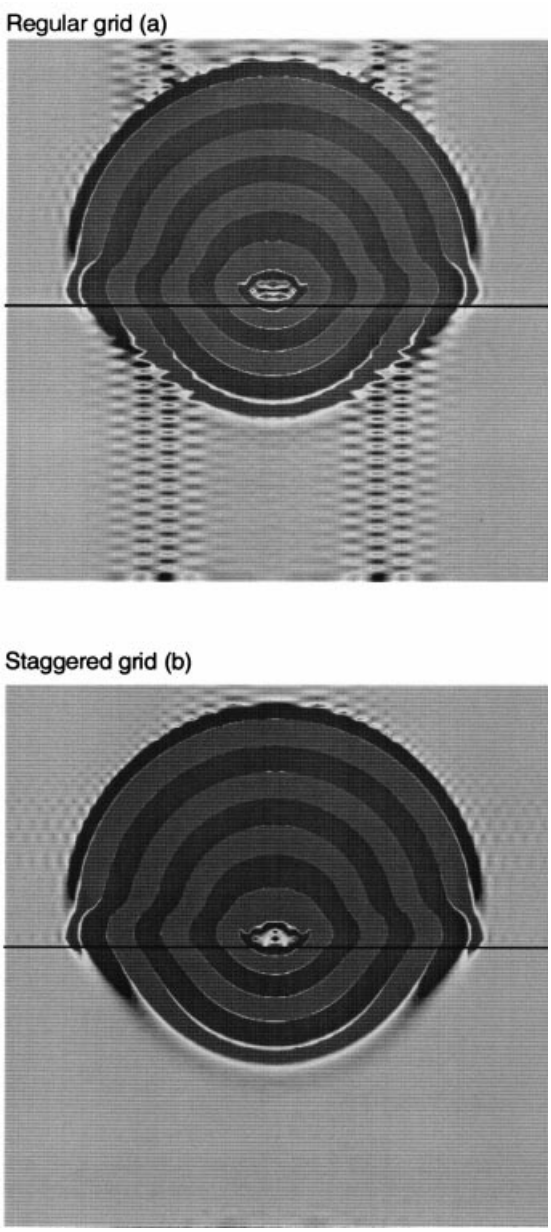

Figure 4. Snapshot of the x-component of the electric field at 7.5 ns on (a) regular and (b) staggered grids, corresponding to Case 4 in Table 1. The source, with a central frequency of 500 MHz, is 30 m above the interface. The signal-to-noise ratio in (a) is approximately 50 dB.

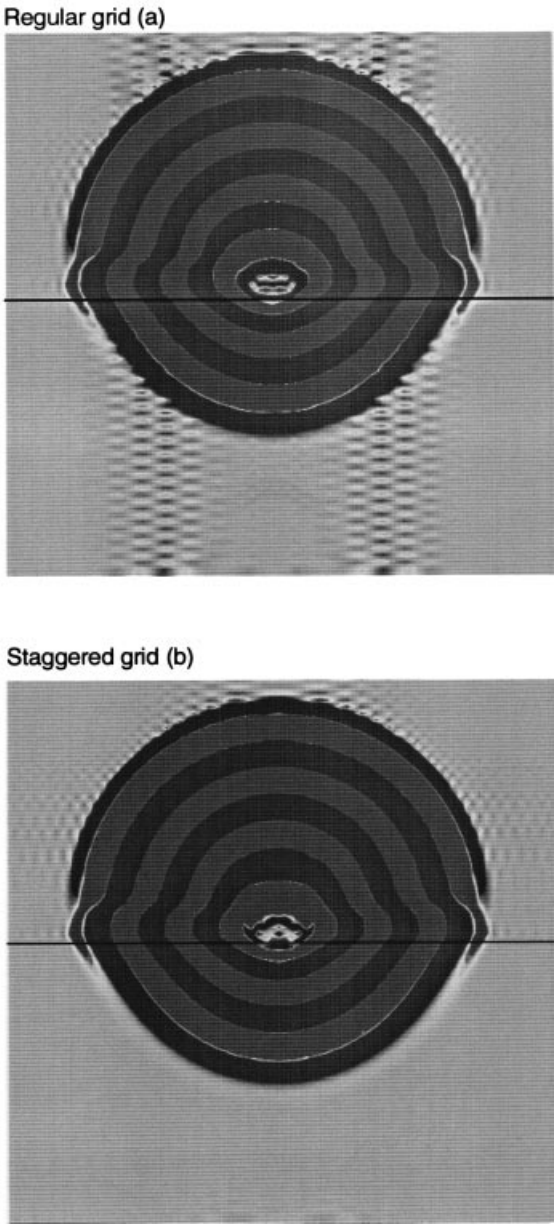

Figure 5. Snapshot of the x-component of the electric field at 7.5 ns on (a) regular and (b) staggered grids, corresponding to Case 5 in Table 1. The source, with a central frequency of 500 MHz, is 30 m above the interface. The signal-to-noise ratio in (a) is approximately 50 dB.

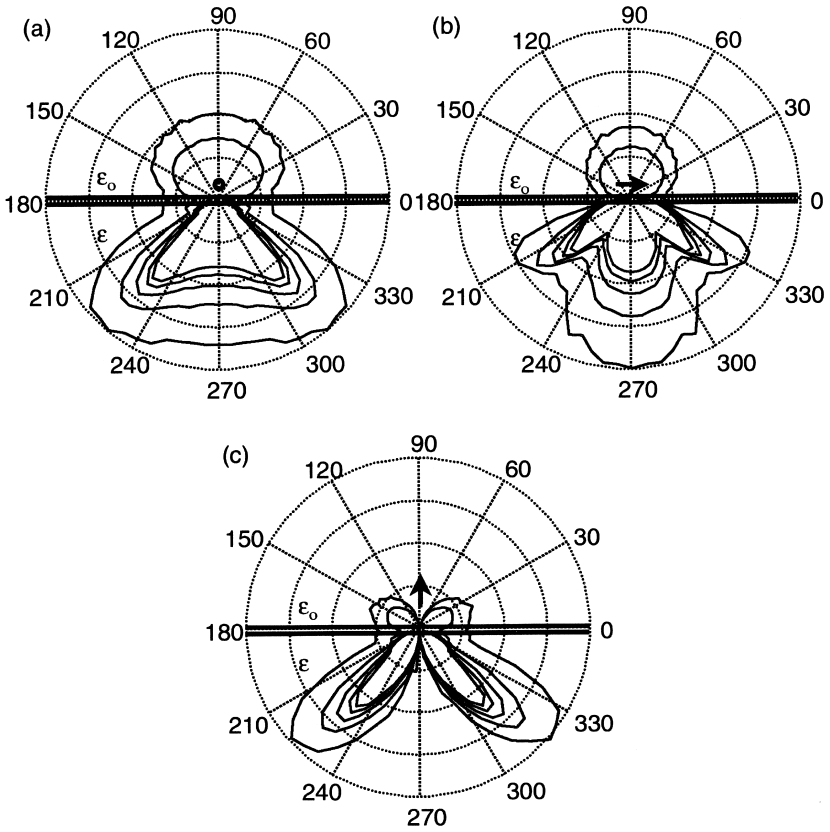

Figure 6. Computed radiation patterns for (a) a magnetic source, (b) a horizontal electric source and (c) a vertical electric source, above an air/solid dielectric interface. The five curves correspond to radial distances of 0.4 m (outer curve), 0.8 m, 1.2 m, 1.6 m and 2 m (inner curve).

dielectric. Figure 6 shows the computed radiation patterns for (a) a magnetic source, (b) a horizontal electric source and (c) a vertical electric source, where the five curves correspond to radial distances of 0.4 m (outer curve), 0.8 m, 1.2 m, 1.6 m and 2 m (inner curve). The patterns, resembling those obtained analytically by Engheta *et al.* (1982) and Smith (1984), are plotted preserving the relative true amplitude.

In the following example, we model the radiation pattern of a 900 MHz GSSI bow-tie bistatic antenna in air (see Fig. 7). The field was measured at a radial distance of 0.5 m, using two sets of antennae. Measurements at greater distances (1 m and 1.5 m) show very similar patterns, such that the measurement, although not in the far-field range, can be considered very close to it. Figure 8 shows (a) the recorded radargrams, (b) the synthetic radargrams obtained with the inversion method in the frequency-domain and transformed to the time-domain, (c) the radargrams simulated with the modelling algorithm, (d) the time histories of the

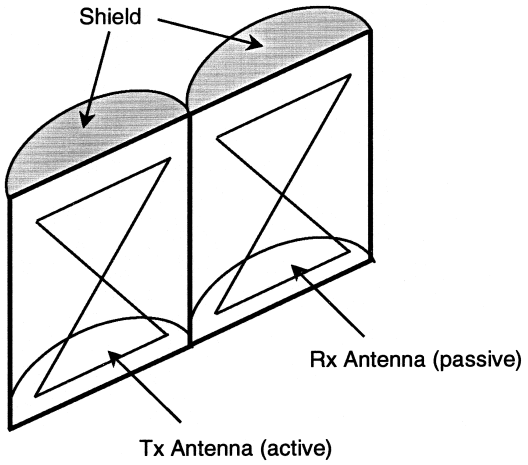

Figure 7. GSSI bow-tie bistatic antenna composed of two dipoles.

single sources, (e) the composite source (three vertical electric dipoles) and radiation pattern, and (f) the snapshot of the magnetic field at 6 ns. The distance between gridpoints in Fig. 8e is 5 cm and the symbols '+' and 'o' correspond to the measured and simulated data, respectively. The pattern is slightly asymmetric since only one of the dipoles operates (see Fig. 7). The presence of the second (passive) dipole and its shield modifies the recorded field. The fit between the measured and modelled radiation patterns yields a residual rms error of 2.3%.

Conclusions

The modelling algorithm for the simulation of electromagnetic radio waves for GPR applications is improved by using the staggered Fourier differential operator and implementing the antenna radiation pattern.

Large contrasts in the material properties cause a series of artefacts when using a regular grid, as, for instance, ringing and acausal events. These problems, due to the non-locality of the differential operator, are almost eliminated by using a staggered grid.

The composite-source concept provides a method of simulating arbitrary radiation patterns from GPR antennae, and of saving computer memory and time by reducing the number of gridpoints used for modelling the antenna. The method simulates the far-field radiated energy with, in general, no more than 9 gridpoints, i.e. a 3×3 region of the numerical mesh. Using this method and a perturbation technique, we have obtained a composite source for simulating the radiation pattern of a 900 MHz GSSI bistatic antenna.

Acknowledgements

This work was financed in part by the European Union under the INCO-COPERNICUS project 'Detection of Hydrocarbon Contaminated Soils by Electromagnetic Techniques', Contract No. ERBIC15CT960801.

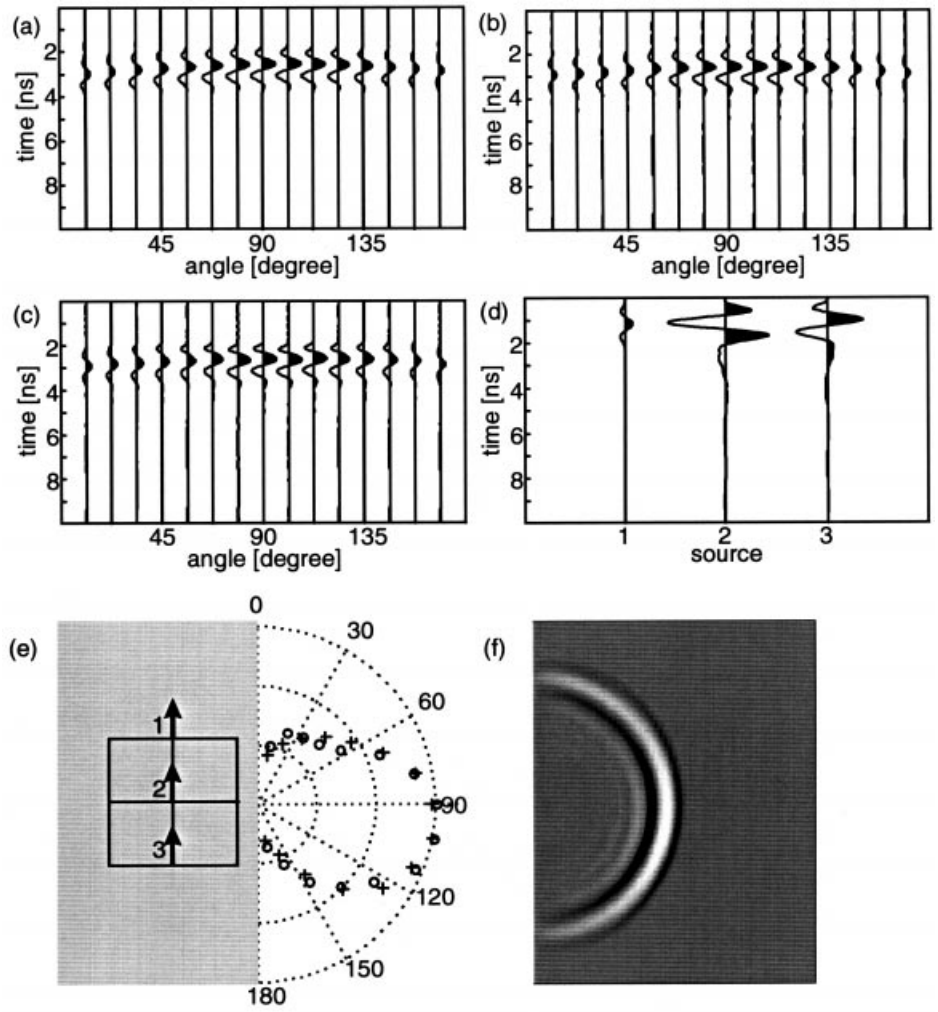

Figure 8. Modelling of the radiation pattern of a 900 MHz GSSI antenna in air: (a) recorded radargrams, (b) synthetic radargrams, (c) radargrams simulated with the modelling algorithm, (d) time histories of the single sources, (e) composite source (three vertical electric dipoles) and radiation pattern, and (f) snapshot of the magnetic field at 6 ns. The symbols '+' and 'o' correspond to the measured and simulated data, respectively.

References

Annan A.P. 1973. Radio interferometry depth sounding: Part I – theoretical discussion. *Geophysics* **38**, 557–580.

Arcone S.A. 1995. Numerical studies of the radiation patterns of resistivity loaded dipoles. *Journal of Applied Geophysics* **33**, 39–52.

Bergmann T. 1998. *Numerical modeling of high-frequency electromagnetic wave propagation*. PhD thesis, University of Kiel, Germany.

Bernabini M., Pettinelli E., Pierdicca N., Piro S. and Versino L. 1995. Field experiments for characterization of GPR antenna and pulse propagation. *Journal of Applied Geophysics* **33**, 63–76.

Bourgeois J.M. and Smith G.S. 1996. A fully three-dimensional simulation of a ground-penetrating radar. *IEEE Transactions on Geoscience and Remote Sensing* **GE-34**, 36–44.

Carcione J.M. 1996. Ground-penetrating radar: Wave theory and numerical simulation in lossy anisotropic media. *Geophysics* **61**, 1664–1677.

Carcione J.M. 1998. Radiation patterns for 2-D GPR forward modeling. *Geophysics* **63**, 424–430.

Chew W.C. 1995. *Waves and Fields in Inhomogeneous Media*. Institute of Electrical and Electronics Engineers, Inc., New York.

Engheta N., Papas C.H. and Elachi C. 1982. Radiation patterns of interfacial dipole antennas. *Radio Science* **17**, 1557–1566.

Fornberg B. 1990. High-order finite differences and pseudo-spectral method on staggered grids. *SIAM Journal of Numerical Analysis* **27**, 904–918.

Harrington R.F. 1968. *Field Computation by Moment Methods*. MacMillan Publishing Co.

Landrø M., Mittet R. and Sollie R. 1993. Implementing measured source signatures in a coarse-grid, finite-difference modeling scheme. *Geophysics* **59**, 1852–1860.

Maloney J.G., Smith G.S. and Scott W.R., Jr 1990. Accurate computation of the radiation from simple antennas using the finite-difference time-domain method. *IEEE Transactions on Antennae and Propagation* **AP-38**, 1059–1068.

Özdenvar T. and McMechan G. 1996. Causes and reduction of numerical artefacts in pseudo-spectral wavefield extrapolation. *Geophysical Journal International* **126**, 819–828.

Özdenvar T. and McMechan G. 1997. Algorithms for staggered-grid computations for poroelastic, elastic, acoustic, and scalar wave equations. *Geophysical Prospecting* **45**, 403–420.

Roberts R.L. and Daniels J.J. 1997. Modeling near-field GPR in three dimensions using the FDTD method. *Geophysics* **62**, 1114–1126.

Smith G.S. 1984. Directive properties of antennas for transmission into a material half-space. *IEEE Transactions on Antennae and Propagation* **AP-32**, 232–246.

Turner G. 1994. Modeling antenna–ground interactions. Proceedings of the 5th International Conference on Ground Penetrating Radar, Kitchener, Ontario, pp. 205–221.

Wensink W.A., Greeuw G., Hofman J. and Van Deen J.K. 1990. Measured underwater near-field E-patterns of a pulsed, horizontal dipole antenna in air: comparison with the theory of the continuous wave, infinitesimal electric dipole. *Geophysical Prospecting* **38**, 805–830.